Micelle-directed chiral seeded growth on anisotropic gold nanocrystals

Micelle-directed chiral seeded-growth on anisotropic gold nanocrystals

Guillermo González-Rubio[1,+], Jesús Mosquera[1,+], Vished Kumar[1], Adrián Pedrazo-Tardajos[2], Pablo Llombart[3,4], Diego M. Solís[5], Ivan Lobato[2], Eva G. Noya[4], Andrés Guerrero-Martínez[3], José M. Taboada[6], Fernando Obelleiro[7], Luis G. MacDowell[3], Sara Bals[2*], Luis M. Liz-Marzán[1,8,9*]

[1] CIC biomaGUNE, Basque Research and Technology Alliance (BRTA), Paseo de Miramon 182, 20014 Donostia-San Sebastián, Spain

[2] Electron Microscopy for Materials Research (EMAT), University of Antwerp, Groenenborgerlaan 171, 2020 Antwerp, Belgium

[3] Departamento de Química Física I, Universidad Complutense de Madrid, Avenida Complutense s/n, 28040 Madrid, Spain

[4] Instituto de Química Física Rocasolano, CSIC, Calle Serrano 119, E-28006 Madrid, Spain

[5] Department of Electrical and Systems Engineering, University of Pennsylvania, Philadelphia, Pennsylvania 19104, USA

[6] Departamento de Tecnología de los Computadores y de las Comunicaciones, University of Extremadura, 10003 Cáceres, Spain

[7] Departamento de Teoría de la Señal y Comunicaciones, University of Vigo, 36301 Vigo, Spain

[8] Ikerbasque, Basque Foundation for Science, 48013 Bilbao, Spain

[9] CIBER de Bioingeniería, Biomateriales y Nanomedicina (CIBER-BBN), Paseo de Miramón 182, 20014 Donostia-San Sebastián, Spain

Abstract:

Surfactant-assisted seeded-growth of metal nanoparticles can be engineered to produce anisotropic gold nanocrystals with high chiroptical activity, through the templating effect of chiral micelles, formed in the presence of dissymmetric co-surfactants. Mixed micelles adsorb on gold nanorods forming quasi-helical patterns, which direct seeded growth into nanoparticles with pronounced morphological and optical handedness. Sharp chiral wrinkles lead to chiral plasmon modes with high dissymmetry factors (~0.20). Through variation of the dimensions of chiral wrinkles, the chiroptical properties can be tuned within the visible and near-infrared electromagnetic spectrum. The micelle-directed mechanism allows extension to other systems, such as the seeded growth of chiral platinum shells on gold nanorods. This approach provides a reproducible, simple and scalable method toward the fabrication of nanoparticles with high chiral optical activity.

One Sentence Summary: Seeded growth of gold nanorods in the presence of micelles with chiral co-surfactants results in nanoparticles with high chiroplasmonic activity.

Chirality is a key signature of nature that can be found across length scales, from subatomic particles, through molecules and biological systems, to galaxies (*1–3*). Imparting handedness to selected materials may provide important advantages in terms of their interaction with living organisms, as well as allow the development of enantioselective catalysts or obtain spin selectivity in electron transport (*4–6*). For example, the demonstration of chiral plasmon modes in noble metal nanocrystals (NCs) has drawn interest in the field of metamaterials and the design of enantioselective sensing probes (*7–9*). The fabrication of plasmonic nanostructures has thus become an active field of research *(10-16).* However, growing crystalline noble metals with dissymmetric morphology is challenging (*10–12*). The formation of chiral plasmonic nanomaterials is usually achieved by means of the assembly of achiral plasmonic gold and silver nanoparticles (NPs) with molecular templates such as DNA, proteins, or polymeric fibers (*13–15*). Although lithographic approaches have been successfully applied to fabricate chiral gold NPs, their scalability remains limited (*9*, *16*).

Advances in the colloidal synthesis of noble metal NPs achieved during the past decades point toward realistic prospects for the production of plasmonic NCs with diverse morphologies, including chiral ones (*17–19*). The presence of chiral amino acids during growth can guide the formation of NCs with distinct handedness. The most prominent example is the synthesis of helicoidal nanostructures assisted by cysteine and glutathione. The enantioselective interaction of amino acids with chiral geometrical elements naturally appearing at particular NC facets has been claimed to induce the observed shape evolution into twisted geometries with high dissymmetry factors (*11*,*20*).

In addition to chiral additives, the synthesis of colloidal chiral NPs requires surface ligands that prevent undesired aggregation (*11*, *21*). However, most of these capping agents also play a role in the growth process and the resulting NC morphology (*17*, *22*). Among the wide variety of ligands used for the synthesis of noble metal NCs, quaternary alkylammonium halide (CTAX, X = Cl, Br) surfactants are some of the most extensively investigated ones. Through the adsorption of CTAX micellar aggregates on certain crystallographic facets, a wide variety of nanoparticle morphologies have been obtained, including nanorods, nanotriangles, and Platonic geometries (*17–19*, *22–24*).

Recently, the addition of co-surfactants such as aromatic molecules, fatty acids, or long chain alkyl alcohols, has been shown to further improve the quality of colloidal gold NPs, and of nanorods in particular (*25–27*). The ability of cosurfactants to intercalate within CTAX surfactant aggregates has been proposed to increase the rigidity of the micelles, induce phase transitions, or both. Interestingly, the impact of co-surfactants on the aggregation behavior of surfactant molecules can also be extended to the formation of chiral micelles. For example, (*R*)-(+)-1,1′-bi(2-naphthol) ((*R*)-BINOL), a co-surfactant with axial chirality (i.e., atropisomerism), can induce the formation of chiroptically active giant worm-like micelles (*28*).

Considering the role of surfactants on the synthesis of gold NCs and the possibility of producing chiral micelles in the presence of BINOL-like co-surfactants, we envisioned the surfactant-assisted seeded-growth of chiral gold NCs. We hypothesized that elongated rod-like particles would have the ideal shape to guide the adsorption of twisted, worm-like micelles on the gold surface into helix-like chiral structures. To investigate both hypotheses, we first carried out a computational analysis on an ideal system comprising cetyltrimethyl ammonium chloride (CTAC) and BINOL. Molecular dynamics (MD) simulations revealed that BINOL molecules induced the assembly of surfactants into chiral wormlike aggregates.

Such elongated micelles tend to coil around gold nanorods, which can thus be considered as templates for the seeded growth of anisotropic NPs with chiral features.

Although experimental evidence of the proposed idea was obtained using BINOL as a co-surfactant, the results of chiral growth were largely improved by using its derivative (*R*)-(+)-1,1′-binaphthyl-2,2′-diamine ((*R*)-BINAMINE)). The growth of plasmonic gold nanorods patterned with a complex chiral surface was indeed confirmed by high-angle annular dark-field scanning transmission electron microscopy (HAADF-STEM) tomography. By tuning the dimensions of the final nanostructures, high anisotropy factors (g-factor ~0.20) were achieved within a wide wavelength range (from 500 to beyond 1350 nm). Theoretical modeling of the optical properties highlights the importance of growing well-defined chiral wrinkles to obtain intense circular dichroism (CD) responses.

MD simulations confirmed that, in the presence of BINOL as a co-surfactant, CTAC can form giant cylindrical micelles that span across the simulation boxes (i.e., up to 60 nm in length; Fig. 1A, fig. S1). Regarding their chiral nature, we observed that unit vectors between the local micellar center and the principal micellar axis were distributed helically; the handedness being dictated by the choice of co-surfactant stereoisomer. This effect can be shown by measuring the average angle formed between pairs of vectors (fig. S2). An achiral helix does not have any tendency to coil into a particular direction, so the angle formed between such vectors averages out to zero.

In our simulations, the average angles not only were finite but appeared sinusoidally correlated and displayed a well-defined handedness (Fig. 1B). Because of the marked atropisomerism of BINOL, we can assume that it could induce helical chirality onto the surfactant aggregates, likely by a sergeants and soldiers mechanism where a chiral molecule directs many achiral molecules or atoms (*29, 30)*. In this case, the adsorbed chiral micelles would assist chirality transfer during further deposition of metal atoms onto the nanorods surface.

We tested this effect by simulating a gold nanorod, immersed in an aqueous mixed solution of CTAB and BINOL. Visual inspection of the simulation results revealed that CTAB and BINOL adsorb into wormlike micelles coiled around the gold nanorod surface (Fig. 1, C and D). Although no preferred orientation of the assembly was observed by the use of different BINOL enantiomers in this case, in the absence of co-surfactant, the coillike morphology was largely lost. Instead, small aggregates and a high fraction of individual surfactant molecules would adsorb on the gold surface (fig. S3). The simulations indicate that chiral wormlike micelles likely formed first and subsequently adsorbed onto the gold nanorod. Thus, a complex cooperative chiral transfer mechanism would convey the atropisomerism from BINOL into the giant micelles and ultimately to gold nanorods.

On the basis of the simulation results, we implemented experimentally the growth of chiral nanorods. (*R*)-BINOL was solubilized by surfactant micelles in aqueous solution, at an optimum molar ratio of 40, and used to template the growth of preformed gold nanorods (130 ± 10 nm long, 29 ± 2 nm thick, see Fig. 2A and SM for details; note that BINOL is insoluble in water in the absence of surfactant). Preliminary characterization by CD spectroscopy revealed the appearance of moderate chiral localized surface plasmon resonance (LSPR) bands (figs. S4 and S5, g-factor ~ 0.002). HAADF-STEM analysis of the NPs grown in the (*R*)-BINOL/surfactant mixture revealed a complex morphology characterized by the presence of wrinkles on the nanorod surface (Fig. 2B and fig. S4). Previous theoretical and experimental studies demonstrated that intense CD responses are exhibited by NPs with distinct chiral distortions, stellated-like morphologies, or both (*9*, *11*, *31*).

Encouraged by the appearance of plasmonic bands in the CD spectra, our efforts focused on improving chiral seeded growth. We hypothesized that the use of stronger stabilizing agents would help directing the growth of more structured chiral wrinkles (*32*). We investigated (*R*)-BINAMINE, an analog of (*R*)-BINOL in which the hydroxyl functionalities are replaced by amine moieties. Although the interaction of amines with gold surfaces is moderately strong (Au–N bond energy ~ 6 kcal/mol), the presence of two amines in a chelating configuration should ensure a greater affinity (*33*, *34*). MD simulations of the BINAMINE/CTAC system confirmed the formation of chiral wormlike aggregates, similar to those for BINOL/CTAC, with a helical distribution of unit vectors (fig. S6). HAADF-STEM analysis of the particles obtained by seeded-growth in (*R*)-BINAMINE/CTAC revealed the presence of gold nanorods displaying a highly complex surface morphology, resembling an intricate network of wrinkles (Fig. 2C, and figs. S7 to 10). Scanning electron microscopy (SEM) imaging of the same NPs also revealed a complex surface structure (fig. S11).

Notwithstanding, proper understanding of such complex structures demands a more detailed characterization than that provided by either HAADF-STEM or SEM, which only retrieve 2D and surface information, respectively. We used HAADF-STEM tomography, which has been shown to be a powerful technique to investigate the three-dimensional morphology of complex NCs. We prepared similar particles, but with increasing dimensions, using 130 nm by 29 nm gold nanorods as seeds and characterized by HAADF-STEM (see SM for synthetic details). Electron tomography reconstructions of nanorods with the smallest degree of growth, i.e. 165 nm long and 73 nm thick, revealed the presence of sharp wrinkles oriented in a seemingly radial direction and displaying tilt angles between 0° and 45° with respect to the short axis (Fig. 2D). Detailed analysis of the internal structure suggested that the wrinkles grew from the surface of the gold nanorod seed, in a quasi-radial direction, up to ~15 to 20 nm in height and with a constant width of 3 to 4 nm. The average intergroove separation was measured to be 2 to 3 nm (Fig. 2E), which is near the 3.75 nm width of wormlike micelles obtained from MD simulations. This finding would point to a micelle-directed chiral growth of the gold nanorods, as we initially hypothesized.

The width of the wrinkles was compatible with the diffusion of metal ion-loaded CTAC micelles from solution (*35*), leading to reduction at available gold sites in between CTAC/BINAMINE micelles on the nanorod surface. By varying the concentration of nanorod seeds in the growth mixture, chiral nanorods were obtained with increased dimensions of 210 nm in length and 112 nm in thickness, and their surface was more entangled (Fig. 2F). Nonetheless, the presence of tilted wrinkles was still visible and angles between 0° and 45° were again observed (between 0° and -45° in the case of (*S*)-BINAMINE, fig. S9). Analysis of the internal structure revealed wrinkles of ca. 35 to 45 nm in height and a similar width to those in the smaller rods (Fig. 2G). Finally, even larger chiral nanorods (270 nm long and 175 nm thick) were investigated. Although the surface appeared more undefined in this case (Fig. 2H), analysis of the internal structure showed the characteristic features described for the previous samples (Fig. 2I). For completeness, 3D animations of all discussed systems are provided as Supplementary Material (Movies S1 to S48).

Diffraction of ideal helical structures results in X-shaped patterns (*36*, *37*). Thus, we applied fast Fourier transformations (FFT) to our 3D reconstructions. We exemplify this analysis with chiral nanorods of 210 nm by 112 nm (Fig. 3, A and B), from which the 3D FFT indeed shows an X-shaped pattern (Fig. 3C); further details are provided in the SM, as well as comparison with an idealized model (fig. S12), with a smooth nanorod (fig. S13) and with a BINOL-grown nanorod (fig. S13). Next, the spots in reciprocal space can be linked to the corresponding features in real space by manually segmenting the 3D FFT to minimize noise. By using the segmented 3D FFT as a mask (see details in SM), an inverse FFT (*38*)

was computed and overlayed (pink fringes) with the original reconstruction, as exemplified in Fig. 3D, so that the helical features are visually highlighted. Although the use of a 3D FFT does not provide a quantitative value such as e.g. the Hausdorff chirality measure (*39*), it provides a qualitative and visual way to estimate the presence of chiral features. The inverse FFT enables direct location of specific periodicities at a local level.

Fringes with a right handed angle can be seen in Fig. 3D, and the wrinkles growing on the sides of the gold nanorod seeds seemed to display a better-defined chiral arrangement than those located at the hemispherical tips. The observation of a curvature-dependent growth was confirmed by a control experiment, in which seeded-growth was carried out on 30 nm gold nanospheres (figs. S14 and S15) Although some chiral features could still be observed, the spheres yielded a more random wrinkle organization, as revealed by the corresponding HAADF-STEM tomography reconstruction (Fig. 2, J and K) and further supported by their 3D FFT and corresponding inverse FFT (fig. S14). Accordingly, more intense plasmonic CD bands were recorded when gold nanorods were used as seeds (g-factor ~0.2, Fig. 4A) as compared to spheres (g-factor ~0.003, fig S15).

Additional evidence behind the general validity of this chiral growth method and the proposed mechanism was provided by experiments in which we varied the nature of the metal deposited during seeded growth. We thus implemented the seeded growth of Pt on BINOL/CTAC-covered gold nanorods, using identical dimensions and similar growth conditions. Representative results are shown in Fig. 3, E to H, show that seeded growth resulted in strikingly regular wrinkled platinum coating. The smaller dimensions of the wrinkles, as well as the different electron configuration between platinum and gold (see a 3D EDX reconstruction in fig. 3E, right), allow a better distinction of the obtained pattern. Although the tilting angle is obviously lower than that measured for gold, a helical character is demonstrated by the 3D-FFT analysis (Fig. 3G and H). Unfortunately, the lossy character of platinum does not allow to record meaningful plasmonic optical activity for these samples.

We next demonstrate that the optical activity (CD bands) can be modulated by varying the dimensions of chiral nanorods (by varying the amount of seeds in the growth solution). In all cases, an intense negative Cotton effect was recorded for the (*R*)-enantiomer (*29*). As the size of the nanorods was increased from 165 nm by 73 nm to 270 nm by 175 nm, the positive band redshifted from 700 up to 1300 nm, and the maximum of the negative band shifted from 1100 to beyond 1350 nm (fig. S16). Analysis of the anisotropy factor showed values ranging from 0.1 to 0.2 (Fig. 4A), which are among the highest values reported for colloidal plasmonic NPs in the visible and NIR ranges (*10, 11*). By extending the analysis further into the NIR, up to the limit of our CD spectrometer (1600 nm), we recorded even higher dissymmetry factors of 0.25 to 0.28 (fig. S17). However, the noise in the 1400 to 1500 nm range precluded us from obtaining more compelling evidence to confirm the precise values.

When gold nanorods of different dimensions and degrees of anisotropy were used to seed the chiral growth (fig. S18 and S19), similar trends in optical activity were observed. However, the anisotropy factor was influenced by the nanorod dimensions. In general, slightly lower g-factor values were obtained when shorter and thinner gold nanorods were used as seeds (100 nm by 12 nm; i.e., higher aspect ratio), while a decrease was observed for seeds with similar length to the optimal one but thicker in diameter (135 nm by 52 nm; i.e., lower aspect ratio).

The relation between the chiral features observed by electron microscopy and the chiroptical activity measured by CD spectroscopy was further investigated by electromagnetic modeling. We used an accurate full-wave solver based on Maxwell's surface integral

equations and the method of moments to model the plasmonic properties of chiral gold nanorods (see SM for details) (*40-42*). Three-dimensional computer-aided design (CAD) models were constructed on the basis of the information provided by the experimental electron tomography reconstructions (Fig. 4B). Although suitable reproduction of the observed morphologies appeared challenging, given the intricate network of wrinkles covering the chiral gold nanorod surface, we created models for the three different dimensions characterized by electron microscopy: 165 nm by 73 nm, 210 nm by 112, and 270 nm by 175 nm. To mimic the regions with wrinkles displaying different angles, each rod was built with sixteen helices having four leveled and four inclined steps per pitch (pitch of 90 nm). The wrinkle width was fixed at 3.5 nm and the separation distance between wrinkles was 2.5 nm.

The simulations revealed chiral plasmonic bands that shifted toward longer wavelengths with increasing nanorod dimensions, in agreement with the experimental results (Fig. 4C, fig. S20 to S22). Differences in the anisotropy factors can be attributed to the polydispersity in size and shape of the real sample, as well as the difficulty in modeling the exact morphology of the NPs. Overall, our theoretical model confirmed the origin of the plasmonic chiroptical activity and the importance of sharp wrinkles for the emergence of strong CD responses. Replacement of BINAMINE by L-cysteine did not induce any clear modification on the CD signal obtained for chiral nanorods synthesized with either (*R*)-BINAMINE or (*S*)-BINAMINE. A substantial modification would be expected if the chiroptical properties would stem from the coupling of the chiral molecules with the NP plasmon, rather than from the chiral structural features (fig. S23). (*43*)

We have experimentally demonstrated that chiral gold nanostructures can be readily obtained by seeded-growth of gold nanorods in BINOL/surfactant mixtures, whereas NP colloids with intense CD responses were obtained using BINAMINE/surfactant mixed micelles. The chiroptical properties stem from the formation and stabilization of steep chiral wrinkles. These findings point to a dual role of mixed micelles: (i) templating the growth of steep wrinkles and (ii) the subsequent stabilization of such morphological features.

We propose that the formation of wrinkles during seeded-growth can be explained by the presence of elongated micelles coiled on the gold nanorod seeds, which act as patterns directing the diffusion of micellar aggregates containing gold ions, from the aqueous solution toward the core NC at intermicellar regions. Indeed, the size of micelles in solution would fit the interwrinkle distance on the nanorod surface. However, wrinkle formation is only induced when the rate of gold ion deposition is faster than their diffusion on the surface (*44*). We observed that, upon lowering the concentration of reducing agent (ascorbic acid, from 160 down to 1.6 mM), the CD intensity decreased by an order of magnitude and less defined surface roughness was observed in STEM (fig. S24).

An additional source of surface stabilization is required to preserve the wrinkles after growth. In this case, BINAMINE plays such a role during the growth process, likely because of its two amine moieties in chelating conformation (*33*). When one of the amine groups in BINAMINE was replaced by a hydroxyl moiety, the passivation effect was suppressed and the growth of chiral features was hindered, which resulted in a decrease of CD intensity (fig. S25). Once the growth is completed, addition of a stronger stabilizing agent (e.g., cysteine) is necessary because the adsorption of surfactant micelles is not sufficiently strong and the nanoparticles may slowly reshape, as reflected by the loss of chiroptical properties (fig. S26).

The approach described here for the synthesis of chiral plasmonic anisotropic nanocrystals is simple, reproducible, and holds great potential for large scale production, intrinsic to colloid chemistry methods. Compared with the growth of inorganic chiral

nanostructures based on the direct chemisorption of small additives on the NC surface to induce chiral growth, the micelle-directed growth method relies on the ability of the chiral-co-surfactant to direct the formation of helical micelles. Such supramolecular assemblies have sufficient interaction points with the NPs to effectively transfer their chirality to the NPs during the growth step through a multivalency effect.

References

1. J. Bailey, A. Chrysostomou, J. H. Hough, T. M. Gledhill, A. McCall, S. Clark, F. Ménard, M. Tamura, Circular Polarization in Star- Formation Regions: Implications for Biomolecular Homochirality. *Science* **281**, 672–674 (1998).

2. L. A. Hodge, F. B. Dunning, G. K. Walters, R. H. White, G. J. Schroepfer, Degradation of DL-Leucine with Longitudinally Polarised Electrons. *Nature* **280**, 250–252 (1979).

3. R. E. Franklin, R. G. Gosling, Molecular Configuration in Sodium Thymonucleate. *Nature* **171**, 740–741 (1953).

4. D. Hanein, B. Geiger, L. Addadi, Differential Adhesion of Cells to Enantiomorphous Crystal Surfaces. *Science* **263**, 1413–1416 (1994).

5. T. P. Yoon, E. N. Jacobsen, Privileged Chiral Catalysts. *Science* **299**, 1691–1693 (2003).

6. K. Ray, S. P. Ananthavel, D. H. Waldeck, R. Naaman, Asymmetric Scattering of Polarized Electrons by Organized Organic Films of Chiral Molecules. *Science* **283**, 814–816 (1999).

7. A. S. Karimullah, C. Jack, R. Tullius, V. M. Rotello, G. Cooke, N. Gadegaard, L. D. Barron, M. Kadodwala, Disposable Plasmonics: Plastic Templated Plasmonic Metamaterials with Tunable Chirality. *Adv. Mater*. **27**, 5610–5616 (2015).

8. C. Hao, L. Xu, H. Kuang, C. Xu, Artificial Chiral Probes and Bioapplications. *Adv. Mater.* **32**, 1802075 (2020).

9. J. K. Gansel, M. Thiel, M. S. Rill, M. Decker, K. Bade, V. Saile, G. von Freymann, S. Linden, M. Wegener, Gold Helix Photonic Metamaterial as Broadband Circular Polarizer. *Science* **325**, 1513–1515 (2009).

10. M. Hentschel, M. Schäferling, X. Duan, H. Giessen, N. Liu, Chiral Plasmonics. *Science Adv*. **3**, e1602735 (2017).

11. H.-E. Lee, H.-Y. Ahn, J. Mun, Y. Y. Lee, M. Kim, N. H. Cho, K. Chang, W. S. Kim, J. Rho, K. T. Nam. Amino-Acid- and Peptide-Directed Synthesis of Chiral Plasmonic Gold Nanoparticles. *Nature* **556**, 360–365 (2018).

12. G. Zheng, Z. Bao, J. Pérez-Juste, R. Du, W. Liu, J. Dai, W. Zhang, L. Y. S. Lee, K.-Y. Wong, Tuning the Morphology and Chiroptical Properties of Discrete Gold Nanorods with Amino Acids. *Angew. Chem. Int. Ed*. **57**, 16452–16457 (2018).

13. A. Kuzyk, R. Schreiber, Z. Fan, G. Pardatscher, E.-M. Roller, A. Högele, F. C. Simmel, A. O. Govorov, T. Liedl. DNA-Based Self-Assembly of Chiral Plasmonic Nanostructures with Tailored Optical Response. *Nature* **483**, 311–314 (2012).

14. C.-L. Chen, P. Zhang, N. L. Rosi, A New Peptide-Based Method for the Design and Synthesis of Nanoparticle Superstructures: Construction of Highly Ordered Gold Nanoparticle Double Helices. *J. Am. Chem. Soc.* **130**, 13555–13557 (2008).

15. A. Guerrero-Martínez, B. Auguié, J. L. Alonso-Gómez, Z. Džolić, S. Gómez-Graña, M. Žinić, M. M. Cid, L. M. Liz-Marzán, Intense Optical Activity from Three-Dimensional Chiral Ordering of Plasmonic Nanoantennas. *Angew. Chem. Int. Ed.* **50**, 5499–5503 (2011).

16. A. G. Mark, J. G. Gibbs, T.-C. Lee, P. Fischer, Hybrid Nanocolloids with Programmed Three-Dimensional Shape and Material Composition. *Nat. Mater.* **12**, 802–807 (2013).

17. Y. Xia, Y. Xiong, B. Lim, S. E. Skrabalak, Shape-Controlled Synthesis of Metal Nanocrystals: Simple Chemistry Meets Complex Physics? *Angew. Chem. Int. Ed*. **48**, 60–103 (2009).

18. B. Nikoobakht, M. A. El-Sayed, Preparation and Growth Mechanism of Gold Nanorods (NRs) Using Seed-Mediated Growth Method. *Chem. Mater*. **15**, 1957–1962 (2003).

19. S. Hong, K. L. Shuford, S. Park. Shape Transformation of Gold Nanoplates and their Surface Plasmon Characterization: Triangular to Hexagonal Nanoplates. *Chem. Mater.* **23**, 2011–2013 (2011).

20. H.-E. Lee, R. M. Kim, H.-Y. Ahn, Y. Y. Lee, G. H. Byun, S. W. Im, J. Mun, J. Rho, K. T. Nam. Cysteine-Encoded Chirality Evolution in Plasmonic Rhombic Dodecahedral Gold Nanoparticles. *Nat. Comm.* **11**, 263 (2020).

21. C. A. S. Batista, R. G. Larson, N. A. Kotov. Nonadditivity of Nanoparticle Interactions. *Science* **350**, 1242477 (2015).

22. M. L. Personick, C. A. Mirkin, Making Sense of the Mayhem behind Shape Control in the Synthesis of Gold Nanoparticles. *J. Am. Chem. Soc.* **135**, 18238–18247 (2013).

23. S. E. Lohse, N. D. Burrows, L. Scarabelli, L. M. Liz-Marzán, C. J. Murphy, Anisotropic Noble Metal Nanocrystal Growth: The Role of Halides. *Chem. Mater.* **26**, 34–43 (2014).

24. S. K. Meena, M. Sulpizi, From Gold Nanoseeds to Nanorods: The Microscopic Origin of the Anisotropic Growth. *Angew. Chem. Int. Ed.* **55**, 11960–11964 (2016).

25. L. Scarabelli, M. Grzelczak, L. M. Liz-Marzán, Tuning Gold Nanorod Synthesis through Prereduction with Salicylic Acid. *Chem. Mater.* **25**, 4232–4238 (2013).

26. X. Ye, C. Zheng, J. Chen, Y. Gao, C. B. Murray, Using Binary Surfactant Mixtures to Simultaneously Improve the Dimensional Tunability and Monodispersity in the Seeded Growth of Gold Nanorods. *Nano Lett.* **13**, 765–771 (2013).

27. G. González-Rubio, V. Kumar, P. Llombart, P. Díaz-Núñez, E. Bladt, T. Altantzis, S. Bals, O. Peña-Rodríguez, E. G. Noya, L. G. MacDowell, A. Guerrero-Martínez, L. M.

Liz-Marzán, Disconnecting Symmetry Breaking from Seeded Growth for the Reproducible Synthesis of High Quality Gold Nanorods. *ACS Nano* **13**, 4424–4435 (2019).

28. T. H. Ito, A. G. Salles, J. P. Priebe, P. C. M. L. Miranda, N. H. Morgon, D. Danino, G. Mancini, E. Sabadini, Generation of a Chiral Giant Micelle. *Langmuir* **32**, 8461–8466 (2016).

29. M. M. Green, M. P. Reidy, R. D. Johnson, G. Darling, D. J. O'Leary, G. Willson. Macromolecular Stereochemistry: The Out-of-Proportion Influence of Optically Active Comonomers on the Conformational Characteristics of Polyisocyanates. The Sergeants and Soldiers Experiment. *J. Am. Chem. Soc.* **111**, 6452-6454 (1989).

30. E. E. Greciano, J. Calbo, J. Buendía, J. Cerdá, J. Aragó, E. Ortí, L. Sánchez, Decoding the Consequences of Increasing the Size of Self-Assembling Tricarboxamides on Chiral Amplification. *J. Am. Chem. Soc.* **141**, 7463–7472 (2019).

31. Z. Fan, A. O. Govorov, Chiral Nanocrystals: Plasmonic Spectra and Circular Dichroism. *Nano Lett.* **12**, 3283–3289 (2012).

32. J. Zhang, M. R. Langille, M. L. Personick, K. Zhang, S. Li, C. A. Mirkin, Concave Cubic Gold Nanocrystals with High-Index Facets. *J. Am. Chem. Soc.* **132**, 14012–14014 (2010).

33. S. Engel, E.-C. Fritz, B. J. Ravoo, New Trends in the Functionalization of Metallic Gold: From Organosulfur Ligands to N-Heterocyclic Carbenes. *Chem. Soc. Rev.* **46**, 2057–2075 (2017).

34. B.-K. Pong, J.-Y. Lee, B. L. Trout, First Principles Computational Study for Understanding the Interactions between ssDNA and Gold Nanoparticles: Adsorption of Methylamine on Gold Nanoparticulate Surfaces. *Langmuir* **21**, 11599–11603 (2005).

35. J. Pérez-Juste, L.M. Liz-Marzán, S. Carnie, D.Y.C. Chan, P. Mulvaney. Electric Field Directed Growth of Gold Nanorods in Aqueous Surfactant Solutions. *Adv. Funct. Mater.* **14**, 571–579 (2004).

36. H. Zhu, K. Suenaga, A. Hashimoto, K. Urita, K. Hata, S. Ijima, Atomic-Resolution Imaging of the Nucleation Points of Single-Walled Carbon Nanotubes. *Small* **1**, 1180–1183 (2005).

37 M. Gailhanou, J. M. Roussel, Diffraction from Twisted Nanowires: Helicity Revealed by Anisotropy. *J. Appl. Cryst.* **24**, 14012–14014 (2003).

38. M. C. Scott, C.-C. Chen, M. Mecklenburg, C. Zhu, R. Xu, P. Ercius, U. Dahmen, B. C. Regan, J. Miao, Electron Tomography at 2.4-Ångström Resolution. *Nature* **483**, 444–447 (2012).

39. J.-Y. Kim, J. Yeom, G. Zhao, H. Calcaterra, J. Munn, P. Zhang, N. Kotov, Assembly of Gold Nanoparticles into Chiral Superstructures Driven by Circularly Polarized Light. *J. Am. Chem. Soc.* **141**, 11739–11744 (2019).

40. D. M. Solís, J. M. Taboada, F. Obelleiro, L. M. Liz-Marzán, F. J. García de Abajo, Toward Ultimate Nanoplasmonics Modeling. *ACS Nano* **8**, 7559–7570 (2014).

41. J. M. Taboada, J. Rivero, F. Obelleiro, M. G. Araújo, L. Landesa. Method-of-Moments Formulation for the Analysis of Plasmonic Nano-Optical Antennas. *J. Opt. Soc. Am. A* **28**, 1341–1348 (2011).

42. D. M. Solís, J. M. Taboada, F. Obelleiro. Surface Integral Equation-Method of Moments with Multiregion Basis Functions Applied to Plasmonics. *IEEE Trans. Antennas Propag.* **63**, 2141–2152 (2015).

43. A. O. Govorov, Z. Fan, P. Hernandez, J. M. Slocik, R. R. Naik, Theory of Circular Dichroism of Nanomaterials Comprising Chiral Molecules and Nanocrystals: Plasmon Enhancement, Dipole Interactions, and Dielectric Effects. *Nano Lett.* **10**, 1374–1382 (2010).

44. Y. Xia, K. D. Gilroy, H.-C. Peng, X. Xia, Seed-Mediated Growth of Colloidal Metal Nanocrystals. *Angew. Chem. Int. Ed.* **56**, 60–95 (2017).

45. T. Altantzis, I. Lobato, A. De Backer, A. Béché, Y. Zhang, S. Basak, M. Porcu, Q. Xu, A. Sánchez-Iglesias, L. M. Liz-Marzán, G. Van Tendeloo, S. Van Aert, S. Bals. Three-Dimensional Quantification of the Facet Evolution of Pt Nanoparticles in a Variable Gaseous Environment. *Nano Letters*. **19**, 477-481 (2019).

46. Zanaga, T. Altantzis, L. Polavarapu, L. M. Liz-Marzán, B. Freitag, S. Bals. A new method for quantitative XEDS tomography of complex heteronanostructures. *Particle & Particle Systems Characterization*, **33**, 396-403 (2016).

47. Goris, W. Van den Broek, K. J. Batenburg, H. H. Mezerji, S. Bals. Electron tomography based on a total variation minimization reconstruction technique. *Ultramicroscopy*, **113**, 120-130 (2012).

48. C. Hanske, G. González-Rubio, C. Hamon, P. Formentín, E. Modin, A. Chuvilin, A. Guerrero-Martínez, L. F. Marsal, L. M. Liz-Marzán. Large-Scale Plasmonic Pyramidal Supercrystals via Templated Self-Assembly of Monodisperse Gold Nanospheres. *J. Phys. Chem. C*. **121**, 10899–10906 (2017).

49. P. Llombart, M. Alzola-Palafox, L. G. MacDowell, E. G. Noya. Structural Transitions and Bilayer Formation of CTAB Aggregates. *Colloids Surf. A* **580**, 123730 (2019).

50. M. A. K. Zuo, L. Breeze, M. Stroet, M. Poger, D. Nair, P. C. Oostenbrink, A.E.C. Mark. An Automated Force Field Topology Builder (ATB) and Repository: Version 1.0. *J. Chem. Theory Comput.* **7,** 4026–4037 (2011).

51. L. Martínez ,R. Andrade, E.G. Birgin, J.M. Martínez. PACKMOL: A Package for Building Initial Configurations for Molecular Dynamics Simulations. *J. Comput. Chem*. **30**, 2157–2164 (2009).

52. G. Bussi, D. Donadio, M. Parrinello. Canonical Sampling through Velocity Rescaling. *J. Chem. Phys*. **126**, 014101–014107 (2007).

53. H. J. C. Berendsen, J. P. M. Postma, W. F. van Gunsteren, A. DiNola, J. R. Haak. Molecular Dynamics with Coupling to an External Bath. *J. Chem. Phys*. **81**, 3684–3690 (1984).

54. H. Heinz, R. A. Farmer, R. R. Naik. Accurate Simulation of Surfaces and Interfaces of Face-Centered Cubic Metals Using 12-6 and 9-6 Lennard-Jones Potentials. *J. Phys. Chem. B* **112**, 17281–17290 (2008).

55. H. Heinz, B. L. Farmer, R. B. Pandey, J. M. Slocik, S. Patnaik, R. Pachter, R. R. Naik. Nature of Molecular Interactions of Peptides with Gold, Palladium, and Pd-Au Bimetal Surfaces in Aqueous Solution. *J. Am. Chem. Soc.* **131**, 9704–9714 (2009)

56. S. K. Meena, M. Sulpizi. From Gold Nanoseeds to Nanorods: The Microscopic Origin of the Anisotropic Growth. *Angew. Chem. Int. Ed.* **55**, 11960–11964 (2016).

57. K. Momma, F. Izumi. VESTA 3 for Three-Dimensional Visualization of Crystal, Volumetric and Morphology Data. *J. Appl. Cryst*. **44**, 1272–1276 (2011).

58. J. M. Taboada, M. G. Araujo, F. Obelleiro, J. L. Rodriguez, L. Landesa. MLFMA-FFT Parallel Algorithm for the Solution of Extremely Large Problems. *Electromagnetics. Proc. IEEE*, ***101***, 350−363 (2013).

59. D. M. Solis, J. M. Taboada, L. Landesa, J. L. Rodriguez, and F. Obelleiro, Squeezing Maxwell's Equations into the Nanoscale. *Prog Electromagn Res.,***154**, 35–50 (2015).

60. P. B. Johnson, R. W. Christy, Optical Constants of the Noble Metals. *Phys. Rev. B*, **6**, 4370−4379 (1972).

61. E. D. Palik, *Handbook of Optical Constants of Solids*; (Academic Press: San Diego, 1985).

ACKNOWLEDGMENTS

Funding: L.M.L.-M. acknowledges funding from the European Research Council (ERC AdG No. 787510). G.G.-R. and J.M. thanks the Spanish MICIU for FPI (BES-2014-068972) and Juan de la Cierva-fellowships (FJCI-2015-25080). S.B., L.M.L.-M., V.K, and A.P.-T. acknowledge financial support from the European Commission under the Horizon 2020 Programme by means of the grant agreement No. 731019 (EUSMI) and the ERC Consolidator Grant No. 815128 (REALNANO). J.M.T and F.O acknowledge financial support from the Spanish MICIU (Grants TEC2017-85376-C2-1-R, TEC2017-85376-C2-2-R), as well as from the ERDF and the Galician Regional Government as part of the agreement for funding the Atlantic Research Center for Information and Communication Technologies (AtlantTIC). AG-M acknowledges financial support from the Spanish MICIU (Grant RTI2018-095844-B-I00), EGN and LGM acknowledge funds from the Spanish MICIU (Grant No. FIS2017-89361-C3-2-P), as well as the use of the Mare-Nostrum supercomputer and the technical support provided by Barcelona Supercomputing Center from the Spanish Network of Supercomputing (Grants QCM-2018-3-0039 and QCM-2019-1-0038). This work was performed under the Maria de Maeztu Units of Excellence Program from the Spanish State

Research Agency – Grant No. MDM-2017-0720. **Authors contributions:** G.G.-R., J.M. and L.M.L.-M. conceived the project. G.G.-R., J.M. and V.K. performed NP synthesis and CD experiments. A. P.-T., I.L., and S.B. carried out EM characterization and analysis. P.Ll., E.G.N. and L.G.M. executed and analyzed MD simulations. D.M.S., E.G.N. J.M.T. and F.O. carried out electromagnetic modeling of plasmonic properties of chiral NPs. G.G.-R., J.M., A.G.-M., S.B. and L.M.L.-M. wrote the manuscript with comments from all authors. L.M.L.-M. supervised the project. **Competing interests:** The authors declare no competing interests. **Data and materials availability:** All data needed to evaluate the conclusions in the paper are presented in the paper or the Supplementary Materials.

Supplementary Materials:
Materials and Methods
Figs. S1-S26
Tables S1-S6
Movies S1-S48
References (45-61)

Figures

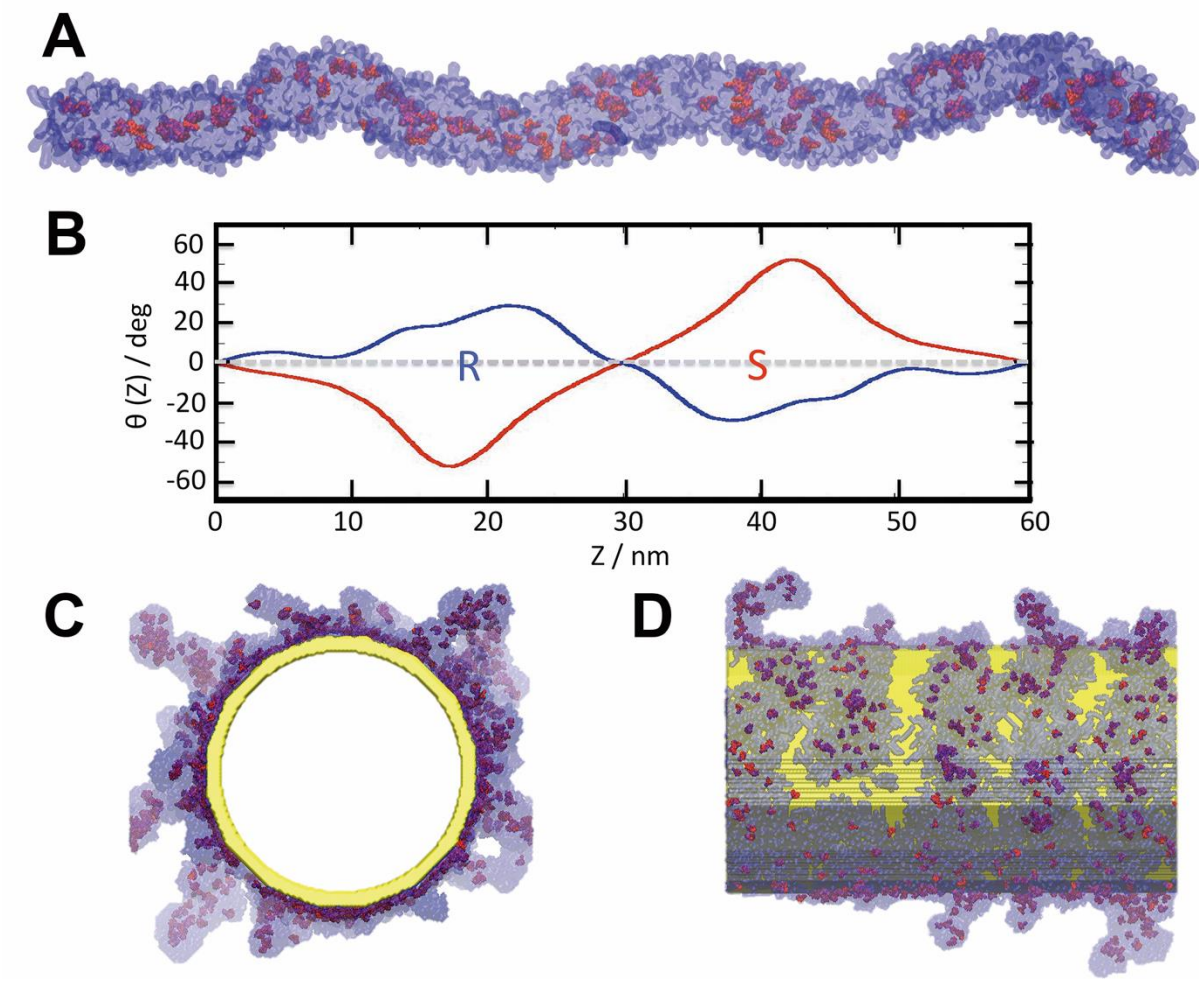

Figure 1. MD simulations of BINOL/CTAC micellar system and their assembly on gold nanorods. (A) MD Simulations for (*R*)-BINOL/CTAC in solution. The aggregation of CTA^+ (blue) in the presence of (*R*)-BINOL (red) results in chiral worm-like aggregates spanning the whole simulation box: 60 nm in length. (B) The shape of the micellar coil is described by a set of vectors along the principal micellar axis. The average angle between vectors is plotted as a function of their vertical distance for 60 nm long rod-like micelles. The presence of (*R*)- or (*S*)-co-surfactant enantiomers in the micelles leads to coiling in opposite directions, as revealed by the sign of the average angle. (C, D) MD simulations for (*R*)-BINOL /CTAC adsorbed onto a gold nanorod in axial and lateral views, respectively.

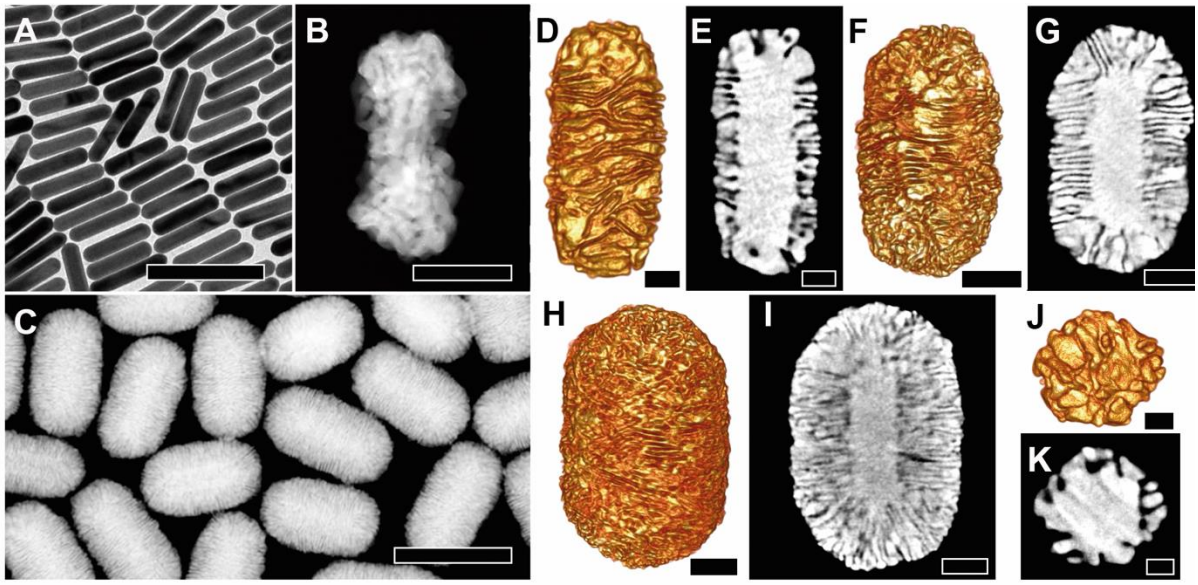

Figure 2. Growth of chiral gold nanorods in micellar systems and effects of size and shape. (A) TEM image of gold nanorods of 130 nm in length and 29 in width, used as seeds. (B) High magnification HAADF-STEM image of a chiral gold nanorod grown in (*R*)-BINOL, displaying a complex surface containing wrinkles. (C) HAADF-STEM image at low magnification of gold nanorods obtained in the presence of (*R*)-BINAMINE, displaying a complex surface containing sharp wrinkles. Scale bars: 200 nm (A,C), 100 nm (B). (D to I) Gold nanorods of 165 nm by 73 nm (D, E), 210 nm by 112 nm (F, G), and 270 nm by 175 nm (H, I) grown in (*R*)-BINAMINE/surfactant mixtures were analyzed by HAADF-STEM. Scale bars: 20 nm (D, E), 50 nm (F, G), 100 nm (H, I) and 10 nm (J, K). Tomography reconstructions (D, F and H) reveal their surface topography, whereas selected orthoslices show the growth of wrinkles from the gold nanorod seeds and the internal structure of the wrinkles network (E, G and I). (J, K) Tomography reconstruction and selected orthoslice of a nanoparticle obtained by overgrowth of a 30 nm gold nanosphere in an (*R*)-BINAMINE/surfactant mixture. Scale bar: 100 nm. Corresponding animated reconstructions are provided in Movies S1 (D), S3 (E), S7 (F), S9 (G), S18 (H), S20 (I), S43 (J) and S45 (K).

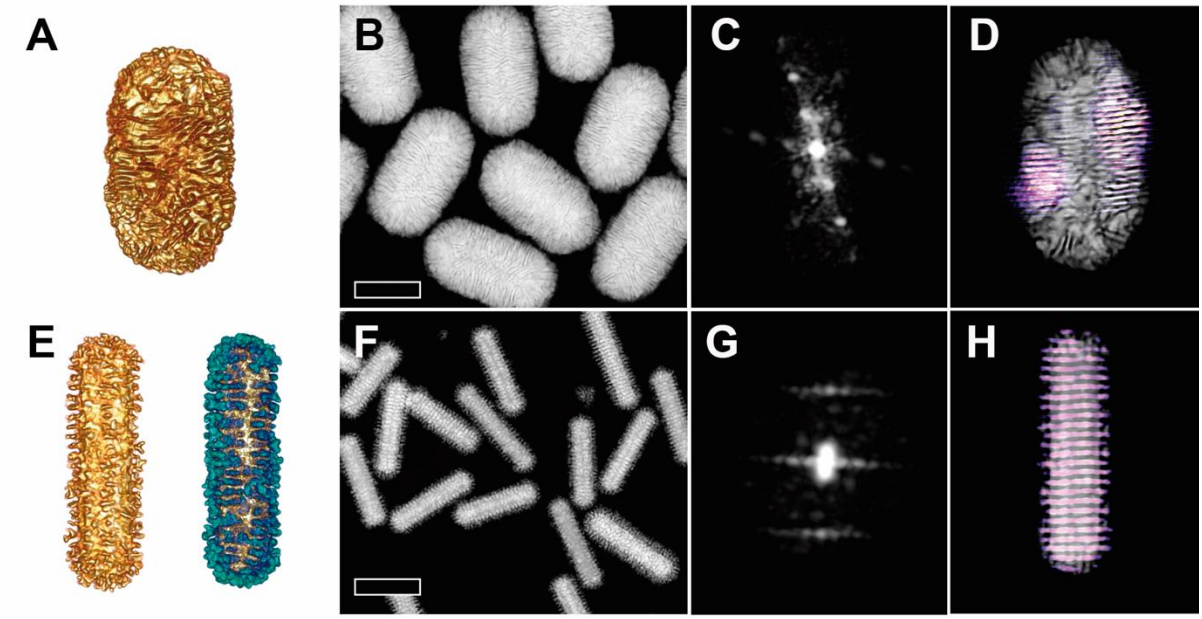

Figure 3. Qualitative analysis of chiral features. (A) Tomography reconstruction of a gold nanorod grown in (*R*)-BINAMINE/surfactant mixture (see also Movie S7). (B) Low resolution HAADF-STEM image of chiral gold nanorods obtained in the presence of (*R*)-BINAMINE. Scale bar: 100 nm. (C) 3D-FFT from which the inverse FFT was computed after segmentation (see also Movie S10). (D) The inverse FFT (see also Movie S12) shows the areas of the particle with chiral features overlapped with the projection of the tomography, indicating a right-handed angle. (E) Tomography reconstruction in HAADF-STEM (left) and EDX (right) modes, of an Au@Pt nanorod grown in (*R*)-BINOL/surfactant mixture (see also Movies S24 and S25). (F) HAADF-STEM image at low magnification of Au@Pt nanorods. Scale bar: 100 nm. (G) 3D-FFT from which the inverse FFT was computed after segmentation (see also Movies S28 and S29). (H) The inverse FFT (see also Movie S30) shows the areas of the particle with chiral features overlapped with the projection of the tomography, indicating a right-handed lower angle.

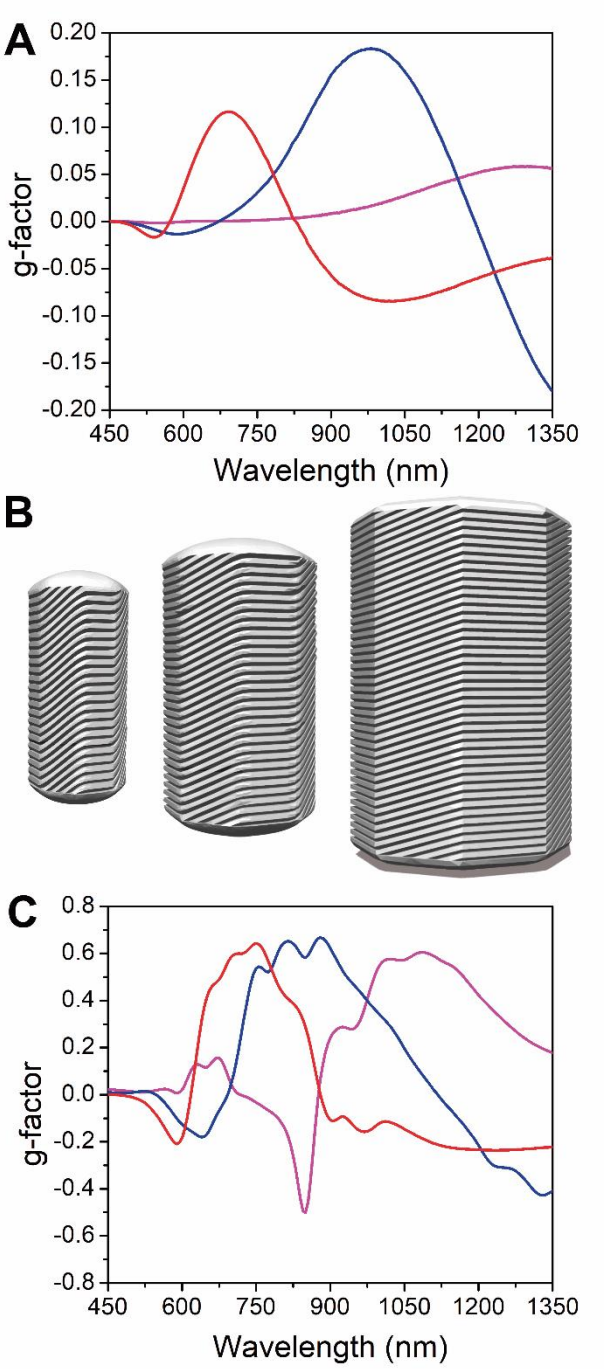

Figure 4. Effect of nanorod dimensions on the chiral plasmonic activity. (A) Spectral evolution of the anisotropy factor for chiral nanorods with increasing particle size: 165 nm by 73 nm (red), 210 nm by 112 nm (blue) and 270 nm by 175 nm (magenta). (B) Models of chiral gold nanorods used to simulate the chiral plasmonic properties (from left to right: 165 nm by 73 nm, 210 nm by 112 nm and 270 nm by 175 nm). (C) Calculated anisotropy factor spectra (from left to right in C: red, blue, and magenta).